Mon. Not. R. Astron. Soc. **000**, 1–17 (2016) Printed 5 April 2017 (MN LaTeX style file v2.2)

Engineering and Science Highlights of the KAT-7 Radio Telescope

A. R. Foley⋆,[1] T. Alberts,[1] R P. Armstrong,[1,2] A. Barta,[1] E. F. Bauermeister,[1] H. Bester,[1] S. Blose,[1] R. S. Booth,[1] D. H. Botha,[3] S. J. Buchner[1,4] C. Carignan[5] T. Cheetham,[1] K. Cloete,[1] G. Coreejes,[1] R. C. Crida,[1] S. D. Cross,[1] F. Curtolo,[1] A. Dikgale,[1] M. S. de Villiers,[1] L. J. du Toit,[3] S. W. P. Esterhuyse,[1] B. Fanaroff,[1] R. P. Fender[2,5] M. Fijalkowski,[1] D. Fourie,[1] B. Frank,[1,6] D. George,[1] P. Gibbs,[1] S. Goedhart,[1] J. Grobbelaar,[1] S. C. Gumede,[1] P. Herselman,[1] K. M. Hess,[5,6,7] N. Hoek,[1] J. Horrell,[1] J. L. Jonas,[1,8] J. D. B. Jordaan,[3] R. Julie,[1] F. Kapp,[1] P. Kotzé,[1] T. Kusel,[1] A. Langman,[1,9] R. Lehmensiek,[3] D. Liebenberg,[1] I. J. V. Liebenberg,[3] A. Loots,[1] R. T. Lord,[1] D. M. Lucero,[5,7] J. Ludick,[1] P. Macfarlane,[1] M. Madlavana,[1] L. Magnus,[1] C. Magozore,[1] J. A. Malan,[1] J. R. Manley,[1] L. Marais,[3] N. Marais,[1] S. J. Marais,[3] M. Maree,[1] A. Martens,[1] O. Mokone,[1] V. Moss,[1] S. Mthembu,[1] W. New,[1] G. D. Nicholson,[10] P. C. van Niekerk,[3] N. Oozeer,[1] S. S. Passmoor,[1] A. Peens-Hough,[1] A. B. Pińska,[1] P. Prozesky,[1] S. Rajan,[1] S. Ratcliffe,[1] R. Renil,[1] L. L. Richter,[1] D. Rosekrans,[1] A. Rust,[1] A. C. Schröder,[11] L. C. Schwardt,[1] S. Seranyane,[1] M. Serylak,[12,13] D. S. Shepherd,[14,15] R. Siebrits,[1] L. Sofeya,[1] R. Spann,[1] R. Springbok,[1] P. S. Swart,[1] Venkatasubramani L. Thondikulam,[1] I. P. Theron,[3] A. Tiplady,[1] O. Toruvanda,[1] S. Tshongweni,[1] L. van den Heever,[1] C. van der Merwe,[1] R. van Rooyen,[1] S. Wakhaba,[1] A. L. Walker,[1] M. Welz,[1] L. Williams,[1] M. Wolleben,[1,16] P. A. Woudt,[4] N. J. Young,[1,4,12] J. T. L. Zwart [5,12]

Affiliations are listed at the end of the paper

Accepted 2016 April 29. Received 2016 April 28; in original form 2015 April 10

ABSTRACT

The construction of the KAT-7 array in the Karoo region of the Northern Cape in South Africa was intended primarily as an engineering prototype for technologies and techniques applicable to the MeerKAT telescope. This paper looks at the main engineering and scientific highlights from this effort, and discusses their applicability to both MeerKAT and other next-generation radio telescopes. In particular we found that the composite dish surface works well, but it becomes complicated to fabricate for a dish lacking circular symmetry; the Stirling cycle cryogenic system with ion pump to achieve vacuum works but demands much higher maintenance than an equivalent Gifford-McMahon cycle system; the ROACH (Reconfigurable Open Architecture Computing Hardware)-based correlator with SPEAD (Streaming Protocol for Exchanging Astronomical Data) protocol data transfer works very well and KATCP (Karoo Array Telescope Control Protocol) control protocol has proven very flexible and convenient. KAT-7 has also been used for scientific observations where it has a niche in mapping low surface-brightness continuum sources, some extended HI halos and OH masers in star-forming regions. It can also be used to monitor continuum source variability, observe pulsars, and make VLBI observations.

Key words: instrumentation:interferometers – radio continuum:general – radio lines:general

1 INTRODUCTION

The seven-dish Karoo Array Telescope array (KAT-7), shown in Figure 1, was built as an engineering testbed for the 64-dish Karoo Array Telescope, known as MeerKAT, which is the South African pathfinder for the Square Kilometer Array (SKA). KAT-7 and MeerKAT are located close to the South African SKA core site in the Northern Cape's Karoo desert region about 80 km north-west of Carnarvon. KAT-7 is remotely controlled from Cape Town, some 800 km away from the site.

The KAT-7 array is extremely compact, with baselines ranging between 26 m to 185 m. The layout was determined using the optimization algorithm described in (de Villiers 2007), which determines a layout for a Gaussian UV distribution given a specified observation setting. The observation setting being optimized in this case was an 8 hour track, with a symmetric hour angle range, on a target at 60 degree declination. The optimization objective was a Gaussian UV distribution at 1.4 GHz, yielding a Gaussian synthesized beam with low sidelobes. Several randomly seeded layouts were generated and were evaluated for a set of observing options ranging in time duration (snapshot, 4hr, 8hr, 12hr) and declination (0, -30, -60, -90 degrees). The layout selected had the lowest sidelobes for the largest number of test observation settings considered. The antenna layout is presented in Figure 2.

The KAT-7 dishes have a prime-focus alt-az design with a focal ratio (F/D) of 0.38, each with a diameter of 12 m, optimized for single-pixel L-band feeds[1]. The low noise amplifiers (LNAs) for the feeds are cryogenically cooled to 80 K using Stirling coolers. The key system specifications for KAT-7 are summarized in Table 1.

The digital backend of the KAT-7 system is an Field Programmed Gate Array (FPGA)-based, flexible packetised correlator using the Reconfigurable Open Architecture Computing Hardware (ROACH [2]), which is a flexible and scalable system enabling spectral line modes covering a wide range of resolutions. Table 2 gives the details of the recently commissioned correlator modes. Digital filters give a flat bandpass over the inner 75% of the band with a rapid roll-off at the edges of the band.

Figure 1. An aerial view of the KAT-7 array; the antennas are pointing towards the south.

Originally, the Karoo Array Telescope was planned to consist of 20 antennas, and the main objective of building a radio telescope was to support South Africa's bid to host the SKA. The original design of the dishes were in fact driven by results from SKA optimization studies (USSKA Consortium 2002). The scope of the project was later expanded to build the 64-antenna MeerKAT array. Before building MeerKAT it was decided to build a smaller prototype array to field-test some of the technologies that might be used in MeerKAT; that array is KAT-7. We note here that science goals for the 7-element array were considered secondary to the design and construction of the array elements. The original scientific considerations for the antenna layout and backend frequency coverage are considered in section 2.

The new technologies implemented and tested on KAT-7 were expected to reduce either capital or running costs when compared to a more 'traditional' radio telescope array. The novel parts included:

- On-site manufacture of single-piece reflectors made of a composite material using a vacuum infusion process. This had an embedded fine wire mesh to act as the radio reflective surface.

⋆ E-mail:tony@ska.ac.za

[1] https://sites.google.com/a/ska.ac.za/public/kat-7

[2] https://casper.berkeley.edu/wiki/ROACH

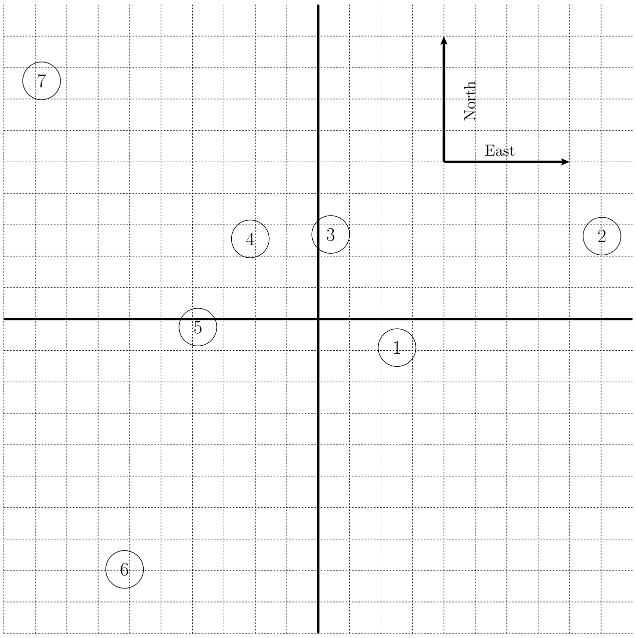

Figure 2. KAT-7, the 7-dish Karoo Array Telescope layout; each block is 10 m and the dish sizes are to scale. The zero point (where the thicker lines cross) is the array centre at $30.7148°$ S, $21.388°$ E.

- A single motor drive per axis with an anti-backlash mechanism and the ball-screw concept for elevation.
- Stirling cycle cooling to cryogenic temperatures (80 K) for the receiver.
- Radio Frequency (RF) over fibre for data transport.
- ROACH boards for all stages of correlation and beamforming.
- Control using the Karoo Array Telescope Control Protocol (KATCP) (see section 6.1).
- Digital data transport in SPEAD (Streaming Protocol for Exchanging Astronomical Data) packets (see section 6.2).

The acquisition and construction phases of KAT-7 began in 2008 with the writing of the telescope requirements specification. ‘First light’ fringes, which were the first successful observations by the interferometer, were obtained between two antennas in 2009. This effectively marked the beginning of the commissioning process. The commissioning and user verification process is complete, and KAT-7 is currently operational.

In addition to hosting the SKA and building MeerKAT, a further focus area of the SKA South Africa project was to embark on a wide-ranging Human Capital Development programme, to ensure that a new generation of scientists and engineers would be available to use the MeerKAT and SKA radio telescopes, and to further science and engineering in South Africa in general. To date many undergraduate and graduate students have been involved in the development of hardware and software for KAT-7 and MeerKAT. Additionally, KAT-7 data has been used at several radio synthesis summer schools in South Africa and in many Honours, Masters, and PhD projects.

This paper is laid out as follows. In section 2 we discuss the reasons for the choice of frequency range for KAT-7. We then detail the antennas and optics (section 3), the Radio Frequency and Intermediate Frequency (RF/IF) chain (section 4), the correlator (section 5) and control systems (section 6). In sections 7–9 we describe some of the early science and commissioning observations. We summarize technology lessons learned and commissioning science results in section 10.

2 CHOICE OF FREQUENCY

One particular scientific niche that was identified for a small-scale interferometer in the southern hemisphere was to make high-sensitivity observations of low surface-brightness emission from extended neutral hydrogen in the nearby Sculptor cluster of galaxies. The interferometer’s response at 1.4 GHz needed to be sufficient to resolve structures on angular scales up to $24'$ (one third of the antenna primary beam). This set the shortest baseline length at 30 m. The positions of the six remaining antennas were selected to optimize the interferometer response for 4-hour observations, resulting in a randomized distribution with longest baseline of 180 m.

The receiver frequency range was chosen to be 1200–1950 MHz in order to avoid potential interference from terrestrial Global System for Mobile Communications (GSM) and aeronautical bands at 960–1164 MHz. The 1.63:1 bandwidth ratio was still feasible with corrugated horn feeds. This frequency range also gave the possibility of joining in with standard 18-cm Very Long Baseline Interferometry (VLBI) observations of OH masers and continuum sources.

3 ANTENNA AND OPTICS

To confirm the suitability of the composite antennas for MeerKAT and the SKA it was necessary to show that they had good aperture efficiency at the highest frequency being considered, and that this lightweight structure could be controlled in standard observing conditions.

To achieve aperture efficiency of 50% at 10 GHz with standard horn feeds (Olver et al. 1994), the unweighted small-scale reflector accuracy was required to be better than 1.5-mm r.m.s. This was achieved by combining theodolite measurements of the completed antennas with finite-element analysis for the worst-case load conditions. Follow-up measurements with radio holography (Scott & Ryle 1977) using a number of geostationary satellite beacons around 11.7 GHz confirmed these results.

The antennas achieve blind pointing accuracy of $25''$ r.m.s. under all but the most extreme operating conditions, with a jitter of no more than $5''$ over time scales of seconds. This is achieved at tracking rates up to 0.05°/sec, across the elevation range. Below 2 GHz the impact on measurements across the antenna beam is no more than 1%, and increases to a maximum of 5.5% at 10 GHz. Optical pointing results show that referenced pointing (Rupen 1997), which involves regularly checking the pointing against a pointing calibration source near the field being observed, may allow accuracies of better than $10''$ to be achieved, which would reduce the impact to 2%. The focal ratio was chosen to be 0.38, which is close to optimal for single pixel feeds using a conical horn feed (Rudge et al. 1982).

A picture of two of the dishes is shown in Figure 3 and dish specifications are shown in table 3. Primary beam measurements at L-band were initially done by total intensity mapping using raster scans across very bright radio sources (in particular Hercules A, Orion A, Taurus A and Virgo A). These were found to be consistent with modeling done by Electromagnetic Software and Systems (EMSS), the company undertaking the receiver systems and optical design. Later the beam shape was measured more accurately using a full polarization holography-like (Scott & Ryle 1977) technique

Table 1. Key performance parameters

Parameters	**Value**
Number of antennas	7
Dish diameter	12 m
Baselines	26 m to 185 m
Frequency Range	1200 MHz–1950 MHz
Instantaneous Bandwidth	256 MHz
Polarization	Linear non-rotating (Horizontal + Vertical) feed
T_{sys}	$<$35 K across the entire frequency band
	($\approx$ 30 K for all elevation angles $>30°$)
Antenna efficiency at L-band	66%
Primary beam FWHM at 1.8 GHz	$1.0°$ [1]
Angular resolution at 1.8 GHz	3 arcmin
Location	latitude $30.7148°$ S, longitude $21.388°$ E, Elevation 1054m
Continuum Sensitivity	1.5 mJy in 1 minute (256 MHz bandwidth, 1σ)
Angular Scales	$3'$ to $22'$

[1]The primary beam FWHM $\theta = 1.27\frac{\lambda}{D}$.

Table 2. Correlator Modes

Mode	**Processed bandwidth/MHz**	**Channel bandwidth/kHz**
Wideband	400	390.625[1]
Beamformer	400	390.625[2]
8k Wideband	400	48.8[3]
HI Galaxy Clusters	400 / 16 = 25	25000 / 4096 = 6.1
HI Large Galaxies	400 / 32 = 12.5	12500 / 4096= 3.0517
HI Galaxies / Maser Search	400 / 64 = 6.25[4]	6250 / 4096 = 1.525879
Maser Monitoring	400 / 256 = 1.5625	1562.5 / 4096 = 0.3814697

[1]The channel bandwidth is obtained by dividing the IF bandwidth (400 MHz) by the total number of channels (1024). Note that only 256 MHz of the IF bandwidth is usable due to RF filtering.
[2]Similar to wideband mode, single boresight beam only.
[3]The IF bandwidth (400 MHz) is divided into 8192 channels.
[4]The usable Bandwidth is slightly less

Table 3. Dish specification

Parameter	**Value**
Pointing Accuracy	$25''$
Surface Accuracy	1.5 mm r.m.s. (spec.)
	1.0 mm r.m.s. (goal)
Specified Upper Frequency Limit	10 GHz
Wind (Operational)	36 km/h
Wind (Marginal Operation) km/h	45 km/h
Wind (Drive to Stow)	55 km/h
Wind (Survival)	160 km/h
Azimuth Rotation slew speed	$2°$/s
Azimuth limits	$-175°$, +285 $°$
Elevation slew speed	$1°$/s
Elevation limits	$0°$, $90°$
Diameter	12 m
Focal ratio f/D	0.38
Lowest Natural Frequency	3 Hz
Feed/Cryo Mass	75 kg
Mount Type	Alt–Az Prime Focus

on the same bright sources (with some dishes tracking while others made spiral scans around the source). The broad features were the same, but the spiral scan mode showed details of the secondary lobes and the instrumental polarization in the primary beam.

3.1 Why composites?

There are three main possible choices for a large dish antenna; a conventional steel structure based on panels, a lighter but possibly more expensive aluminium structure with panels, or a composite dish with metal backing for rigidity. For KAT-7 the choice was made for a composite for the following reasons:

- The dish front surface is constructed as a single unit, which gives it inherent stiffness (more efficient structure), something that is lost when the dish is constructed from loose panels. This is an important aspect which reduces the mass while keeping the stiffness of the dish.
- When constructed as a single unit there are no discontinuities in the reflective surface.
- When constructed as a single unit there is no need to set up and align panels on a backing structure that is off the ground, which could prove to be time consuming and would be required for every dish. Setting up of the mould is only required once, but must be done accurately.
- Combining the composite dish surface with the steel rib and web backing gives a cost-effective solution.
- An infusion process can be used, which is a tried-and-tested technology on such large structures.
- Tooling is relatively inexpensive.

It is also very convenient that the thermal expansion coefficients of the composite dish front and the steel backing are very

Figure 3. Two of the KAT-7 dishes viewed side-on. Note the lightning rods at the apex and near the focus, the backing structure of steel beams with circular holes, the small counterweight on the right and the sun shield on the left hand side of the pedestal.

close to each other, giving low thermal loading. Thermal loading is potentially a large problem for pointing and surface accuracy, given the large temperature changes in the semi-desert climate of the Karoo. In addition the lightweight nature of the dish meant that the counterweight needed would be light and that the motors could be low-powered and still achieve good slew speeds.

The main drawbacks for a composite laminate dish are that the mould accuracy must be higher than that of the desired surface and that the layers of the laminate must be made in a balanced and symmetrical way to reduce the inherently anisotropic nature of the fibre mats. For balance any laminae must be placed symmetrically around a centre line, and for symmetry any laminae at layer (*n*) must have an identical ply at layer (-*n*) from the middle of the layers. For example a minimal set would be weave layers in the sequence $(0,90)^\circ$ $(45,-45)^\circ$ $(45,-45)^\circ$ and $(0,90)^\circ$. This symmetry is straightforward for a circularly symmetrical dish, but more complicated for other shapes, e.g. MeerKAT, which has an offset Gregorian geometry.

4 RF AND IF CHAIN

4.1 Feed

The feed provides native horizontal and vertical linear polarization. Conversion to circular polarization in the receiver is not implemented into the design. Adding a polarizer would have increased the complexity of the receiver, which was considered a risk. Adding the required components (90° hybrid and isolators preceding the low-noise amplifiers) inside the 80 K cryostat with a single stage Stirling cooler would increase system noise by at least 5%. A linear polarization response could be calibrated sufficiently well to meet the 30-dB linear and circular polarization purity required for e.g. measurements of Zeeman splitting; making a feed for a large fractional bandwidth ($> 30\%$) while retaining accurate circular polarization is difficult.

4.2 RFE Architecture

The Radio frequency Front End (RFE) architecture of KAT-7 is shown in Figure 4. The design was driven by the following design decisions:

- Reduce complexity of the RFE at the antenna focus to reduce self-generated radio frequency interference (RFI) to the maximum extent possible, in preference to mitigating RFI later.
- Reduce complexity of the RFE at the antenna location and move the down-converter and clock distribution to the same location as the digitiser.
- Test the concept of mitigating RFI by moving the digitiser away from the antenna location to a shielded container located about 6 km away, with the Losberg mountain providing a very high order of RFI shielding.

It is a double heterodyne system involving fixed and variable local-oscillator (LO) signals that translate an RF (in the frequency band of 1.2–1.95 GHz) to an IF signal (in the band of 72–328 MHz) compatible with the digital samplers. The first local oscillator (LO1) can be set in the range 5.5–6.1 GHz while the second (LO2) is fixed at 4.0 GHz. The mixing scheme is shown in Figure 5. Figure 6 gives details of the last stage of down-conversion and suppression of aliasing. 'BPF's are bandpass filters and 'ADC's are analogue to digital converters.

4.3 Noise Diodes

Each receiver includes two stabilized noise diodes to permit online monitoring of system noise and receiver gain. The period and the duty cycle of the noise system can be software selected, as well as having a simple on/off mode. The signal can either be added to the received ('sky') signal via an antenna that is integrated into the feed horn ('the pin') or via 3-dB couplers that are installed between the OrthoMode Transducer (OMT) ports and the low noise amplifiers ('the coupler'). The 'pin' signal level is approximately equivalent to the system temperature (T_{sys}) while the 'coupler' level is approximately $\frac{T_{sys}}{10}$. Using the 'coupler' it is possible to calibrate total-power measurements to an absolute scale with accuracy better than 10%. The 'pin' injection was designed to allow delay and phase calibration between the orthogonal linear polarization channels while the antennas were operating in single-dish mode, and has been rarely used since the array was functional. The receivers were designed to permit observations of the Sun. However, no 'high' noise diode is provided to allow such observations to be calibrated.

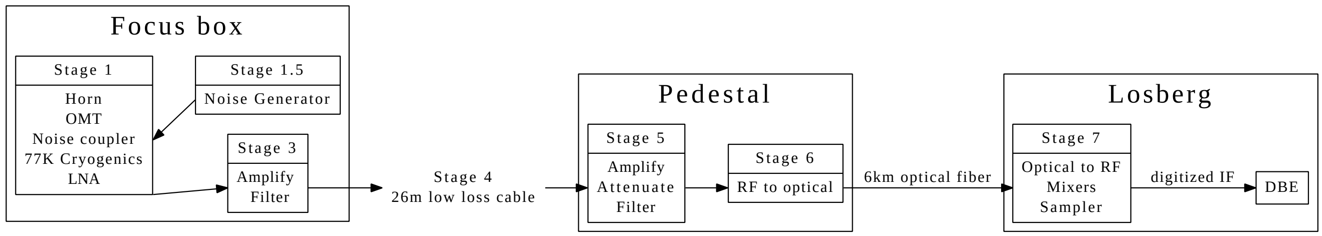

Figure 4. Signal chain from receiver to Digital Back End (DBE). Signals arrive at the horn and go through the OrthoMode Transducer (OMT) to the Low Noise Amplifier (LNA). Calibration from a noise generator can be injected. After further amplification and filtering they descend to the pedestal where they are again amplified. The signal level is adjusted by attenuators and the signals is then filtered and used to modulate an optical signal. This is transmitted over optical fibre and converted back to an RF signal in the Losberg facility. This then is mixed with local oscillators and digitally sampled for the Digital Back End

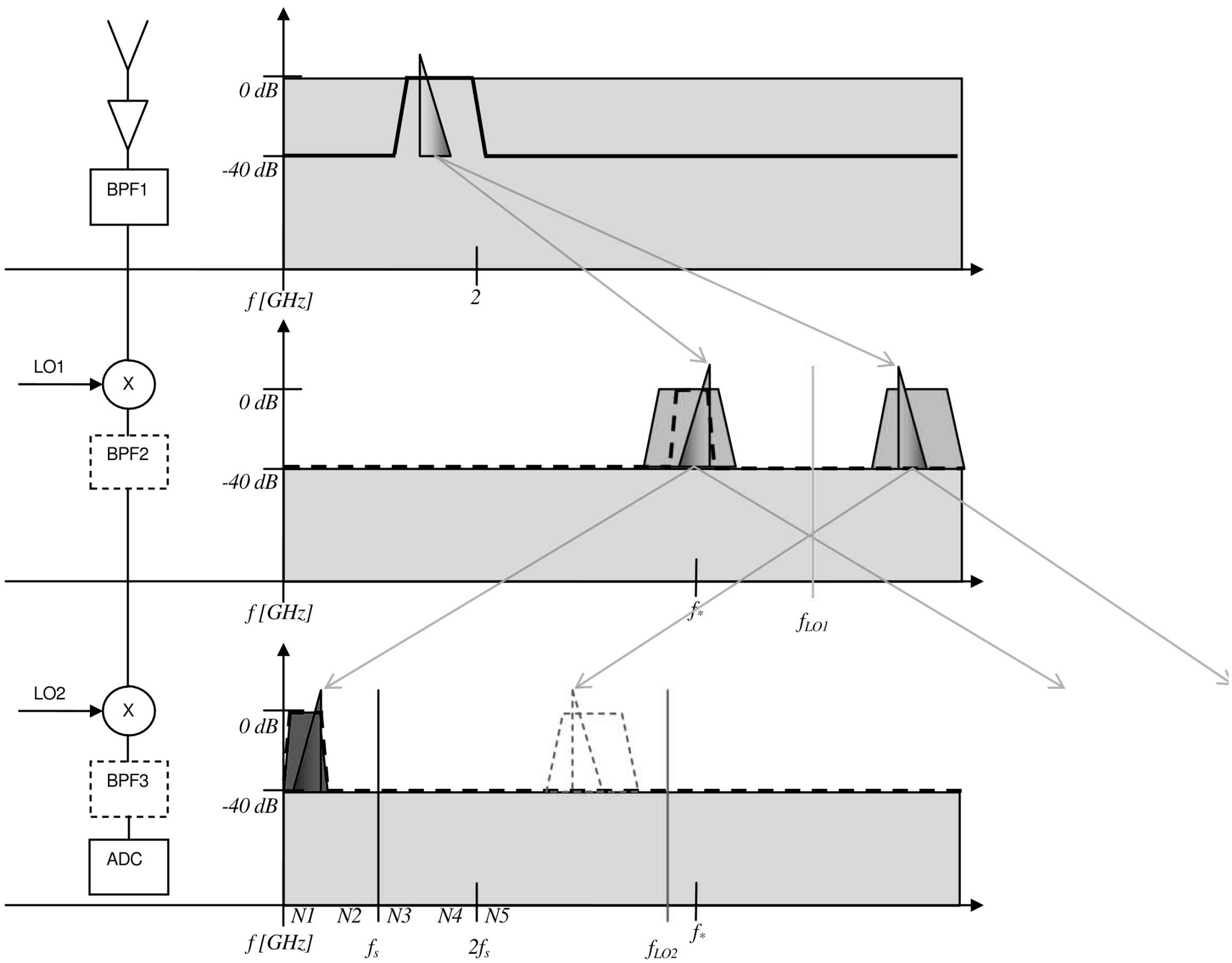

Figure 5. An illustration of the down-conversion and sampling procedure. On the left side is the signal chain (top to bottom) with bandpass filters BF1-BF3, local oscillators LO1 and LO2 and the Analogue to Digital Converter (ADC). f_{LO1} and f_{LO2} represent frequencies of the local oscillators. On the right are the spectra at the various stages. The top spectrum shows the signal as it arrives at Losberg, the middle spectrum shows the signal (and its alias) after mixing with LO1, while the bottom spectrum show the signal (and alias) after mixing with LO2, just before it is sampled by the ADC. N1 to N5 are the Nyquist zones.

4.4 Down-conversion and Digitisation

To reduce the risk of RFI at the antennas, the analogue RF signal is transported via fibre-optic cables to a central facility behind Losberg mountain. The signals are then down-converted using a common LO, after which they are sampled in baseband (i.e. first Nyquist zone). The nominal signal is sampled with 3 bits (r.m.s. $\approx$ 3 levels) using 8-bit samplers. Together with the 27 dB of headroom to the 1-dB compression point provided by the end-to-end analogue line-up, this provides the high dynamic range that is required to limit the response to strong interfering signals. Even on occasions when navigation satellites traverse the antenna beam, gain compression remains at or below the 1% level so intermodulation products remain undetectable.

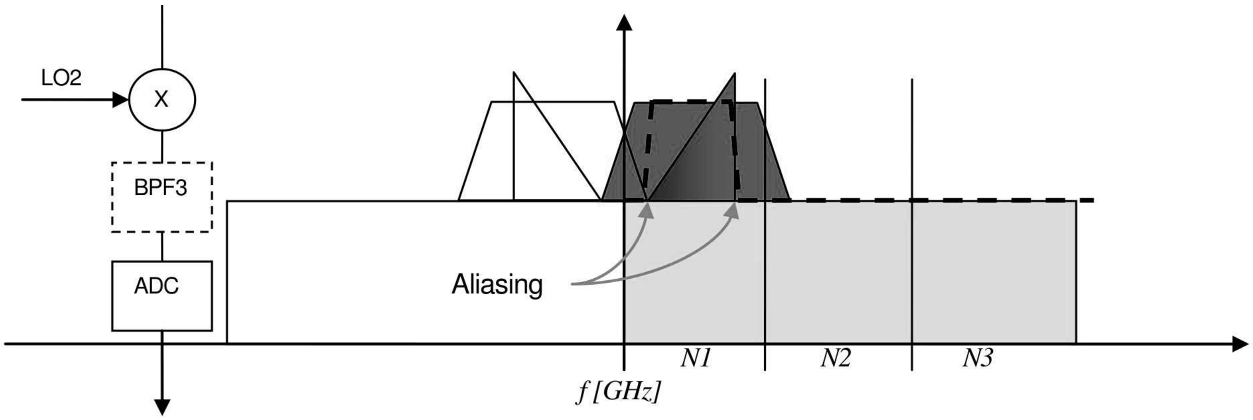

Figure 6. Detail of the last stage of the down-conversion procedure, showing the last (fixed) local oscillator, LO2, and possible aliasing. The bandpass filter (BPF3) is designed to reduce that aliasing to a minimum before it enters the ADC, so that it does not appear in the sampled data. N1-N3 represent different Nyquist zones

The analogue chain was designed to limit instrumental phase instability to less than 8° r.m.s. over 30-minute time scales. A Global Positioning System (GPS)-disciplined Rubidium maser clock is employed as frequency reference to which the LOs are phase-locked. This allows the system to achieve adequate phase stability to limit VLBI coherence loss to 20% at frequencies up to 2 GHz.

5 CORRELATOR

The correlator modes are noted in Table 2. The correlator is based on the so-called 'FX' architecture (Fourier transform 'F' followed by Cross-correlation 'X') with Hann-windowed polyphase filter banks (PFBs).

The spectral-line modes are limited to a single band per observation, which is a minor inconvenience for observations of OH maser lines. The correlator always computes all four complex polarization products for all baselines (including autocorrelations) since, with linearly-polarized feeds, total-power measurements are easily corrupted by linear polarization and therefore polarization calibration is required to achieve the highest possible fidelity total-power imaging.

The correlator performs all internal computations with sufficient numerical precision to support a spectral dynamic range of 43 dB.

The Digital Back-End (DBE) also provides a coherently-summed beamformer in parallel with a wide-bandwidth correlator. The beamformer voltages are channelized to coincide with the correlator's 390 kHz-wide channels. This correlator output is used by the Science Processing Team's online pipeline to keep the array phased-up during the course of the observation. The Science Processor also provides the facility to re-synthesize and re-sample the channelized voltages to the bandwidths required for the observation. The beamformer's output may be used for VLBI recording or for performing coherent de-dispersion of pulsar signals. Figure 7 shows a simplified block diagram of KAT-7's prototype correlator, consisting of three main components:

- The *F-engines* which channelise the incoming data streams into spectral components.
- The *X-engines* which multiply and accumulate every product pair.
- A commodity, off-the-shelf network switch to interconnect these boards.

KAT-7 required additional features to turn the basic correlator into a more fully-featured digital back-end, most notably beamforming (for tied-array operation) as well as additional operations in the correlator itself such as fringe rotation and delay compensation, fast readout speeds and a standardised output protocol. Hardware changes were also required: The performance of the existing digitisers within the Collaboration for Astronomy Signal Processing and Electronics Research (CASPER[3]) collaboration were found to be inadequate for KAT-7, and there was a desire for KAT-7 to standardise on a single, general-purpose hardware processing platform that could both digitise and process the signals.

In its current form, the KAT-7 DBE consists of 16 ROACH boards, eight of which are configured as F-engines and the remaining eight as X-engines. It is a real-time, full-Stokes, asynchronous packetized design with 16 inputs, processing 400 MHz of RF bandwidth (only 256 MHz of which contains useful analogue signal because of the anti-aliasing filters introduced in the RF chain (see Figure 6). ROACH boards can optionally host ADCs for digitising analogue signals and the F-engines in KAT-7 are equipped with KAT ADCs to digitise the down-converted IF signal at 800 MSample/s with an 8-bit resolution. A 20-port 10 GbE network switch is used to interconnect all the processing boards.

While the F-engines and their ADCs are synchronously clocked from a GPS-disciplined rubidium common clock source, the X-engines are purely compute nodes that operate from their own, asynchronous, clocks. Packets are timestamped in the F-engines and these headers are interrogated by subsequent processors for data identification and re-alignment. These X-engines could easily be replaced by ordinary Central Processing units (CPUs) and Graphical Processing Unit (GPUs) when technology advances enable them to cope with the data rates presented.

The fringe rotation and delay compensation were implemented within the F-engines by employing a combination of time-domain and frequency-domain processing, and the system currently allows for phased-tracked wideband (continuum) and spectral-line observations. It does not allow online Doppler tracking.

[3] `https://casper.berkeley.edu`

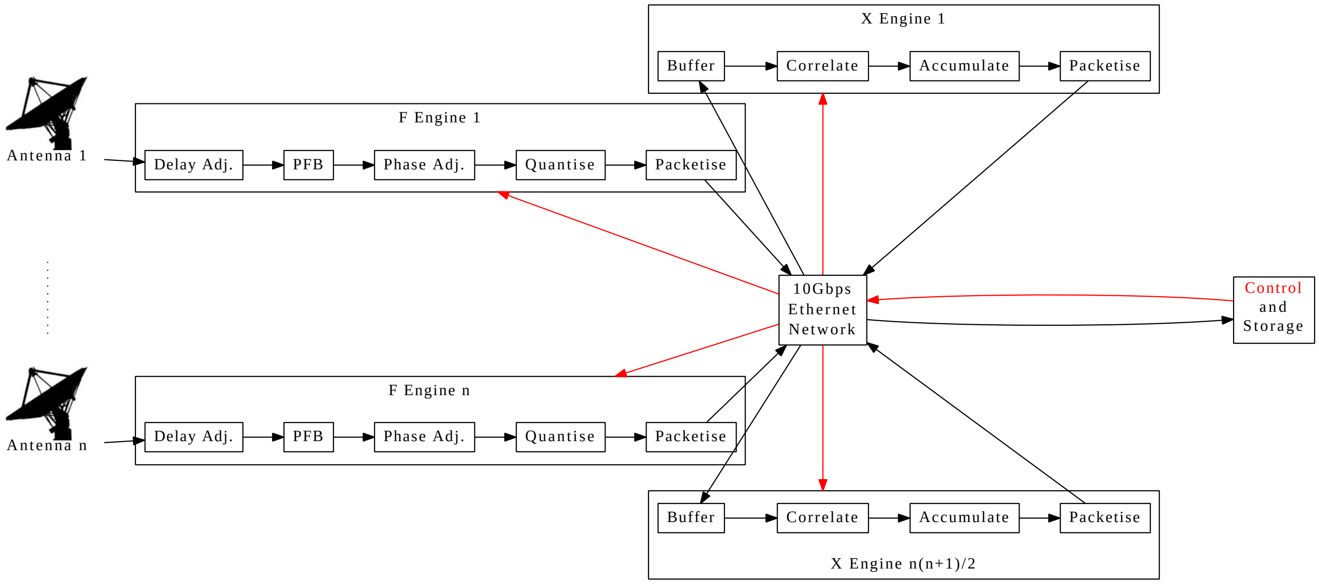

Figure 7. The KAT-7 Correlator. The signal chain (in black) for two of the telescopes is shown, as well of the control and monitoring (in red). The F-engines do the Fourier transform and X-engines do the correlations. For n antennas there are $\frac{n(n+1)}{2}$ correlation products if you include all autocorrelations. For simplicity we consider only one polarization here.

Frequency-domain beamforming is implemented by tapping a copy of the channelised data destined for the X-engines, and presenting it to a co-located *B-engine* which performs beam steering and summation. The existing F-engines are thus shared by the X- and B-engines. Development time and risk were reduced by leveraging the existing delay-compensation software. This B-engine is not resource hungry, needing only a single complex multiplier and adder to sum the already serialised data, along with a lookup table for the steering coefficients. This makes it possible to create additional beams with modest incremental hardware costs.

All systems are being designed to be directly transportable and up-scalable to larger arrays such as MeerKAT and the SKA.

6 CONTROL

6.1 The KAT Control Protocol: KATCP

The MeerKAT telescope contains a large number of devices that require control and monitoring, usually both. Most of these devices are bespoke, meaning that they were constructed either within the project or by a contractor to the specifications defined by the project. As a consequence we had the luxury of being able to select a communications design strategy, architecture and protocol suite used for the control and monitoring of the telescope.

A significant design decision was to confine low-latency, real-time control functions to a small set of components. In other words the control system as a whole does not operate on a low-latency basis — instead, time critical commands are sent out well in advance (with a time stamp in the future at which they are to be performed) and are scheduled by a smaller real-time component close to the limited number of elements requiring such control. The system distributes a clock signal to subordinate nodes. This decision makes it possible to use computer systems running conventional (not hard-real-time) operating systems that communicate using common, non-deterministic interconnects and protocols. In particular it was possible to select transmission control protocol (TCP)/Internet protocol (IP) over Ethernet for transport: these are well-established, pervasive and inexpensive lower communications layers.

The only locally developed part of the control network is the application control protocol, KATCP, running on top of TCP/IP. KATCP borrows from established, classical Internet protocols such as Simple Mail Transfer Protocol (SMTP), File Transfer Protocol (FTP) and Post Office Protocol (POP) in that it is an application protocol which is easily read by humans; each line of text is a protocol message. The protocol is not too different from a command prompt or shell interface, where each input line is also a command. However, unlike command line utility output, the protocol replies have a regular, well-defined structure[4].

6.2 Streaming Protocol for Exchanging Astronomical Data: SPEAD

In analogy with the control protocol, we unified the data exchange protocol wherever practicable. Hence the correlator internals, correlator output stage, and science processor all share a common data-exchange format called SPEAD[5].

SPEAD is a one-way, best-effort, self-describing protocol, containing both machine and human-readable descriptions. This allows receiver processes to automatically unpack data, enabling application designers to concern themselves with algorithms rather than with data exchange. It also allows users to comment their data-streams so that stored data can easily be reinterpreted at a later date without additional documentation, or to easily debug data exchanges.

[4] See `https://casper.berkeley.edu/wiki/KATCP` and `https://pythonhosted.org/katcp`.
[5] The specification document and a full description can be found at `https://casper.berkeley.edu/wiki/SPEAD`

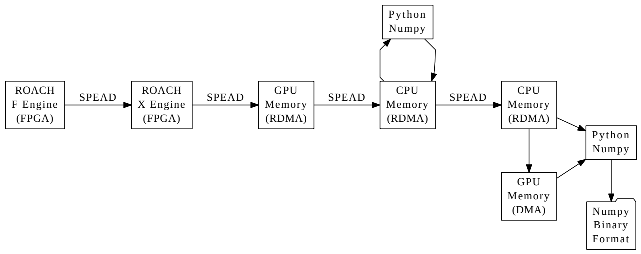

Figure 8. SPEAD exchanges between a range of platforms. Once the data are sampled and Fourier transformed in the F-engine all the data are handled internally as SPEAD packets or as Numpy arrays.

Other data protocols such as the VLBI Data Interchange Format (VDIF [6]), were considered, but it was decided that they were not sufficiently self-describing or flexible.

SPEAD was developed in collaboration with the PAPER (Precision Array for Probing the Epoch of Reionization; Parsons et al. 2010) team as part of the broader CASPER collaboration and is available under an open-source GNU general public license. SPEAD can be used for on-the-wire exchange, for on-disk storage or for piping data between application processes within a single compute node. This protocol is implemented on ROACH boards, CPUs, and GPUs.

SPEAD is in essence optimised for the transmission of arrays of data from one location to another. In particular we use SPEAD extensively for the movement of PYTHON NUMPY [7] arrays (Figure 8). It is designed to allow exchange of arbitrary data structures and aims to keep receivers' copies fresh by propagating any changes to the receiver as these changes occur on the transmitter. The metadata and variable descriptors are injected into the primary data stream. Such changes will occur if the correlator is started, or changes mode, or the frequency of an LO is altered. Receiver processes keep state information, so the latest values of all variables within the structure are always available, even if only the changed subset is transmitted. If these dynamic features are not required, a lightweight and faster static implementation can be made.

As a one-way transport, and because it operates over the User Datagram Protocol (UDP) on Ethernet networks, it is easy to support multicast transparently, allowing multiple devices to subscribe to the same data-streams. This allows real-time data inspection and plotting by subscribing to a subset of the data. As UDP does not check for packet delivery, SPEAD was made to tolerate some packet loss, but cannot request a lost or corrupted packet. Buffering helps by allowing for packets being received out of sequence.

7 FIRST IMAGE WITH KAT-7

The first tests of the completed KAT-7 system were undertaken in 2011 August using the Wideband continuum mode (See Table 2). The specific combination of sensitivity, angular resolution, $\approx 3(4)'$ at 1822(1328) MHz, and field-of-view ($\approx 1^\circ$) of KAT-7 require extended southern sources as imaging targets to use for testing this mode. One such source is PKS 1610-60 which has an extent of $30'$ in right ascension and $4'$ in declination (Christiansen et al. 1977).

[6] `http://www.vlbi.org/vdif/`
[7] `http://www.numpy.org`

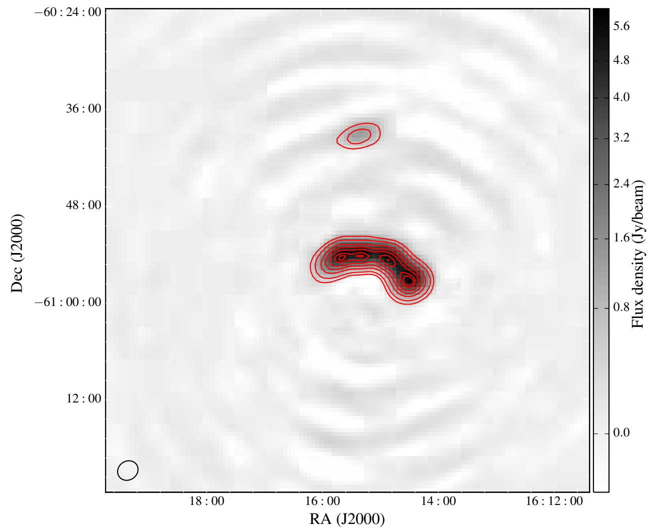

Figure 9. Synthesis image of PKS 1610-60 region containing the more prominent bent-double radio galaxy PKS 1610-60.8 (below) and the smaller radio galaxy PKS 1610-60.5 (above). Contours start at 0.5 Jy and increment by 1 Jy, with an additional contour at 1 Jy to better delineate PKS 1610-60.5.

This source was observed with KAT-7 for 10 hours with both polarizations at a frequency of 1822 MHz. The KAT-7 correlator outputs the data into an observatory-specific format based on HDF5. After conversion to a standard Measurement Set the data are calibrated and imaged in CASA (McMullin et al. 2007). The final total-intensity image can be found in Figure 9. The dynamic range (ratio of the peak image intensity of 6.06 Jy to the r.m.s. image noise of 0.03Jy) of this map is about 200:1. We find a total integrated flux density of 30.9±3.1 Jy for PKS 1610-60.8 and 1.6±0.2 Jy for the smaller radio galaxy PKS 1610-60.5. The measured fluxes are consistent with values listed in the Parkes Southern Radio Catalog (extrapolated from 1410 GHz assuming a spectral index $\alpha = 0.7$ where $S \propto \nu^{-\alpha}$; Wright & Otrupcek (1990)).

8 RADIO CONTINUUM IMAGING AND MONITORING

A sample of calibrators ($-90^\circ < \delta < 30^\circ$) are continuously being monitored and identified as possible short-spacings flux-density calibrators (Kassaye 2014). The aim of this monitoring campaign is also to image potential new calibrators with short spacings and to assess their long-term variability. Several sources that are suitable as point-source calibrators for interferometers with larger dishes, and consequently smaller fields-of-view (such as e.g. J0943-081 and J2326-4027) have proven unsuitable for KAT-7 as they have nearby contaminating sources within the primary beam. In general we have rejected candidate calibrators that have a contaminating source above 10% of their peak brightness, or where the integrated flux density (estimated using the shortest baseline) is more than 10% greater than the maximum flux density per beam. Given the size of the KAT-7 primary beam at 1.2 to 1.95 GHz, most maps have few hundred milliJansky spread over a number of sources brighter than 1mJy/beam. This is consistent with source number counts from the FIRST (White et al. 1997) and ATLBS (Subrahmanyan et al. 2010) surveys. With the modest angular resolution of KAT-7 we would expect our images to be limited by confusion noise rather than thermal noise in Stokes *I*. For most places on the sky we reach a continuum confusion limit of about 1(2) mJy/beam at 1822(1328) MHz (based on no more than one source per five beams), and making high dynamic range continuum images where confusion is so high has proven difficult. The confusion limit is even higher along the Galactic plane.

From a full-polarization analysis, the polarization fraction of $8.4 \pm 0.6\%$ was seen for 3C286 and $8.1 \pm 0.6\%$ for 3C138. These values are consistent with those determined by Perley & Butler (2013). Polarization was calibrated using full-Stokes observations of unpolarized radio sources such as PKS 1934-638 to determine instrumental leakage (of total intensity into polarization), and sources with high linear polarization at L-band over a large range of parallactic angles to measure delay and phase offsets between horizontal and vertical dipoles. Typical leakages within the half-power beam width were of the order of 3% in the upper band (1822 MHz) and 3-6% in the lower band (1322 MHz), so second-order correction effects were negligible.

Although the dynamic range in continuum total intensity is limited by confusion after about 8 hours, this is not the case for polarization or spectral-line observations. However, the instrumental polarization corrections are needed for high dynamic range spectral line observations, such as in OH maser observations.

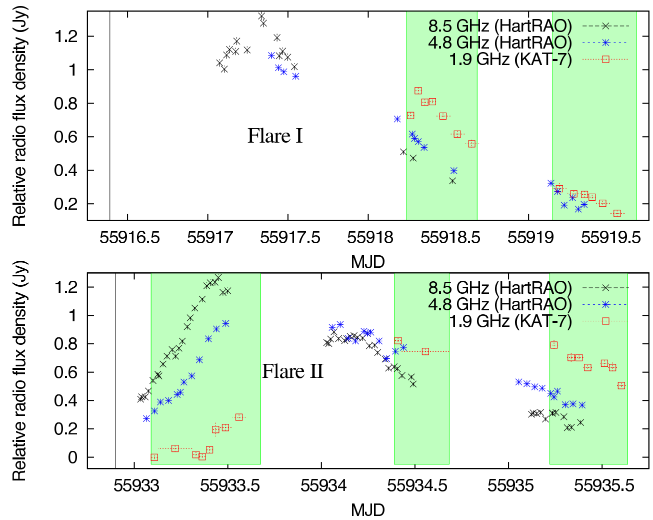

Figure 10. A radio light curve of Circinus X-1 obtained with KAT-7 (1.9 GHz, red crosses) and HartRAO (4.8 GHz, black circles and 8.5 GHz, blue stars). The X-ray binary system is clearly flaring to Jansky levels again. The times in which KAT-7 is operational are shown in green. The vertical bars at each point represent the measurement noise, while the horizontal bars represent the observation length.

9 COMMISSIONING SCIENCE WITH KAT-7

KAT-7 went through a science commissioning phase. The requirements for commissioning science projects are (i) that they test the performance of various aspects of commissioning (e.g. correlator modes, data reduction pipeline, RFI mitigation), and (ii) they endeavour to contribute new and original scientific results. These projects touch on a broad range of scientific interest, including, but not limited to, topics identified as MeerKAT Key Science Projects. Projects include:

- Monitoring variable continuum sources (selected from the Astronomer's Telegram (ATEL) announcements).
- Imaging extended, diffuse continuum emission.
- Timing strong southern pulsars.
- Conducting very long baseline interferometry (VLBI).
- Measuring HI spectral line kinematics and low surface brightness emission in nearby galaxies and clusters.
- Monitoring OH maser emission.
- Mapping large scale polarization.

We outline several of these completed and ongoing science commissioning projects in the following subsections. We highlight their scientific importance, and their contributions to KAT-7 commissioning and preparations for MeerKAT.

9.1 Transient sources

Many transient sources have been monitored with KAT-7 ranging from neutron-star and black-hole X-ray binaries, blazars, Galactic gamma-ray binaries, and novae. In this section we highlight several of these observations.

Long-term monitoring of Circinus X-1, a bright and highly variable X-ray binary, was carried out during 2011 December 13 to 2012 January 19 using KAT-7 wideband continuum mode at 1.9 GHz and the HartRAO radio telescope at 4.8 and 8.5 GHz (Armstrong et al. 2013).The observations confirm a return to strong radio flaring first observed in 1970's that had been suppressed for two decades. Figure 10 shows this long-term behaviour. This is the first published scientific paper using KAT-7 data, and a good example of multi-wavelength collaboration between South African instruments.

Simultaneous observations of the black hole candidate Swift J1745-26 with KAT-7, the Very Large Array (VLA), and the Australia Telescope Compact Array (ATCA) radio interferometers reveal a 'failed outburst' event, illuminating details of the complex processes of accretion and feedback in black holes (Curran et al. 2014). The KAT-7 observations were carried out using the wideband continuum mode at a center frequency of 1.822 GHz over 13 epochs from 2012 September 13 to November 11.

PKS 1424-418, a known blazar, was observed with KAT-7 as a follow-up to ATEL4770 (Ciprini & Cutini 2013). At a redshift of $z = 1.522$, this source has shown multiple flaring events in optical and γ rays in 2009-2010 (Hauser et al. (2009), Hauser et al. (2010), Longo et al. (2009) and Donato (2010)). Tingay et al. (2003) showed that the source also shows variability in the radio regime. On 30th January 2013 it was reported in ATEL 4770 (Swift detection of increased X-ray activity from gamma-ray flaring blazar PKS 1424-418; Ciprini & Cutini (2013)) that PKS 1424-418 went through a γ-ray outburst and that the X-ray flux was increasing (as it had done this in the past). This motivated us to obtain follow up observations with KAT-7 to search for variability in the radio wavelengths. We observed PKS 1424-418 using the wideband continuum mode at a center frequency of 1822 MHz for 3.9 hrs on the 3 July 2013. The primary beam corrected total intensity map is depicted in Figure 11. The r.m.s. noise in the image ranges from 8.5 mJy/beam near the phase center to 14.0 mJy/beam near the edge of the primary beam. We measure a total flux of 3.9±0.4 Jy for PKS 1424-418, consistent with the expected flux at the observed frequency for the target in its quiescent non-flaring phase (Tingay et al. 2003). All continuum emission located within the primary beam with a peak above 6σ of the r.m.s. noise are real non-variable radio sources and their fluxes are consistent with those extrapolated from a Sydney University Molonglo Sky Survey (SUMSS) image (assuming a typical spectral index of

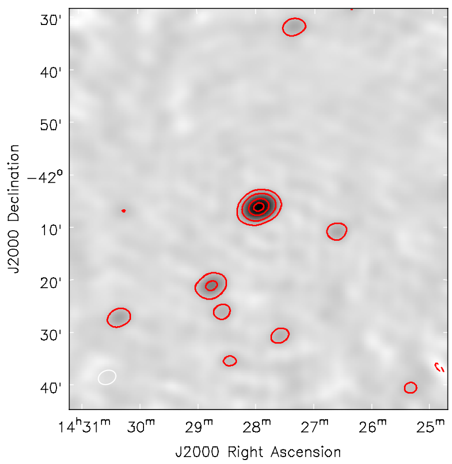

Figure 11. Primary beam corrected image of PKS 1424-418 imaged after ATEL4770. Contours are -6, 6, 36, 180, and 360 times the r.m.s. noise of 8.5 mJy/beam. Negative contours are shown dashed and the synthesized beam is shown in the bottom left corner. The full width half maximum of the primary beam is 57.5 arcminutes. All emission with a peak above 6 sigma of the r.m.s. noise are real non-variable radio sources and their fluxes are consistent with those extrapolated from a Sydney University Molonglo Sky Survey (SUMSS) image (assuming a typical spectral index of 0.7 for synchrotron emission).

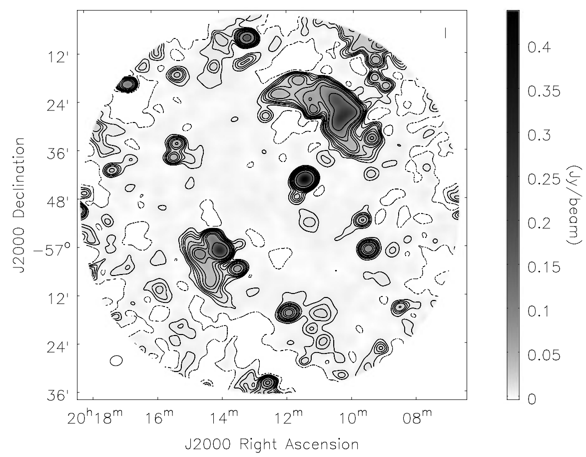

Figure 12. Total intensity map of Abell 3667 at 1826 MHz. Image noise is 1.30 mJy/beam. Contours mark [-1,1,2,3,4,6,8,12,16,32,64,128] $\times\sigma_{\rm rms}$. The synthesised beam size (empty circle bottom left) is $184 \times 150''$. The FWHM of the primary beam is 1.0°. The depicted region extends out to 10% of the primary beam. Figure adapted from Riseley et al. (2015).

0.7 for synchrotron emission; Mauch et al. (2003)). For instance for PKS 1425-421 (14h28m45.0s; -42d21m15s) we measure a total flux of 0.42±0.4 Jy and the extrapolated SUMSS flux at 1822 MHz is 0.44±0.01 Jy.

A campaign to monitor another another blazar source, PKS 1510-089, began on 21 October 2011 and lasted two years (Oozeer et al. 2015). PKS 1510-089 is a flat spectrum radio loud quasar at a redshift of $z = 0.361$ and has been extensively observed from the radio to gamma wavelengths (Marscher et al. (2010); D'Ammando et al. (2009); D'Ammando et al. (2011); Saito et al. (2013); Lazio et al. (2001)). The KAT-7 data were obtained using the wideband continuum mode at a center frequency of 1.822 GHz over 38 epochs with a cadence of at least once a month. The integration time of each observation varied from 3 to 12 hours. The r.m.s. noise of each observation ranged from 0.5 mJy beam^{-1} to 2 mJy beam^{-1}. At least one flaring event was successfully observed during this campaign (see Figure 2b of Oozeer et al. (2015)). The peak flux at quiescence is 2.1 Jy and the peak flux at the peak of the flaring event is 3.3 Jy.

9.2 Diffuse radio emission

With the availability of short spacings (26–185 m, see Table 1), KAT-7 is an ideal instrument to detect extended diffuse radio emission especially in galaxy clusters hosting halos and relics. One such cluster is Abell 3667, one of the most well-studied galaxy clusters in the Southern Hemisphere. It hosts two giant radio relics and a head-tail radio galaxy (Rottgering et al. 1997). Recent work suggests that a bridge of diffuse synchrotron emission connects the north-western radio relic with the cluster center (Carretti et al. 2013). To investigate the nature of the diffuse radio emission from the relics and 'bridge' of the cluster we observed Abell 3667 with KAT-7 in March 2013. The observations were done using the wideband continuum mode at a center frequency of 1826 MHz. Nine closely packed pointings were used to cover the entire cluster region. The mean time per pointing was 70 minutes. The mean r.m.s. noise per pointing is 1.4 mJy beam^{-1}. The pointings were mosaiced during deconvolution and imaged out to 10% of the primary beam ($\simeq 1°$at 1826 GHz). As seen in Figure 12, the nature of the diffuse emission (two large-scale relics) was confirmed, but only patchy low-level flux is observed between the central galaxy and the north-west relic. This patchy emission is spatially coincident with several point sources that appear in the SUMSS catalogue (Mauch et al. 2003). A more detailed analysis of these data can be found in Riseley et al. (2015).

9.3 Pulsars

KAT-7 high time-resolution capability was first demonstrated through a $\simeq$ 2 min single-dish observation of the Vela pulsar (PSR J0835−4510) in late 2012. These data were channelised into 1024×0.396 MHz channels giving full 400 MHz bandwidth and were sampled at the Nyquist rate of 2.56 μs. The data were then funnelled from the KAT-7 beamformer and written to disk using a high-performance multiplexing algorithm to cope with data-throughput requirements. A custom pipeline, based on DSPSR digital signal processing software (van Straten & Bailes 2011)[8] was used to produce total-intensity, PSRFITS[9] format data offline. PSRCHIVE, a scientific data analysis software library was used for further processing and analysis of these data (Hotan et al. 2004)[10].

Semi-regular dual-polarisation observations of bright pulsars ($\gtrsim$ 10 mJy) using KAT-7 frequency-domain beamforming abilities have since become standard practice. Phase-delay correction for these observations is performed in a two-step procedure: 1) coarse-delay correction through application of the known geometrical de-

[8] http://dspsr.sourceforge.net/
[9] http://www.atnf.csiro.au/research/pulsar/index.html?n=Main.Psr
[10] http://psrchive.sourceforge.net/

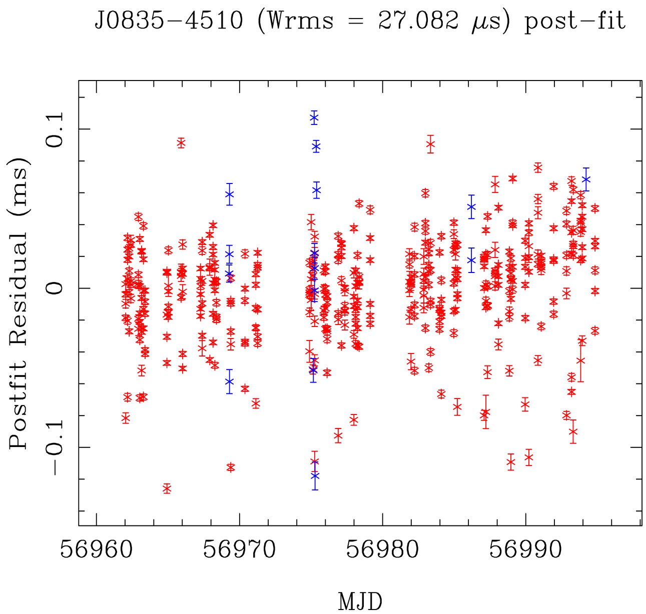

Figure 13. Timing residuals for the Vela pulsar (J0835−4510) over an approximately 38 day span of data. Measurements obtained with the HartRAO 26-m telescope (red crosses) were carried out almost daily and typically lasted 1 min. These observations were centred on 1668 MHz with a bandwidth of 150 MHz. Those obtained with KAT-7 (blue crosses) were obtained on 4 separate days only, with a typical duration of 5 min. The KAT-7 observations were dual polarization with a bandwidth of 200 MHz and made use of all seven antennas. These data confirm that the timing accuracy of the two telescopes is comparable.

lays between antennas and 2) fine-delay correction across the band. The latter is performed through observation of a bright calibrator source that is used to optimise the X/B-engine complex weights. Beam-steering is subsequently performed in the X/B-engines to produce a single, boresight beam per polarisation on the sky.

These observations rely on the same offline processing pipeline to produce data in PSRFITS format, with at least 512 bins per pulse period, from the Nyquist-sampled, channelised voltage data from the beamformer. Due to data-storage limitations, so-called half-band mode is used where only the central 200 MHz of the observing band (i.e. 512 frequency channels) is retained, as well as observing time ranges typically between 5 and 15 min[11].

Single-pulse and folded search capabilities have successfully been demonstrated using a number of known sources. A series of short pulsar-timing campaigns has also been undertaken, predominantly focusing on the Vela pulsar due to its low period (~ 89.3 ms) and high flux density (1.1 Jy at 1400 MHz; Backer & Fisher (1974)). Fig. 13 shows a comparison between the timing residuals obtained in 2014 November for PSR J0835−4510 using HartRAO and KAT-7 data. Fig. 14 shows averaged profiles for a number of pulsars produced via our custom data pipeline.

9.4 VLBI

Pathfinder VLBI observations are critical to the establishment of the African VLBI Network (AVN; Gaylard et al. (2011)) in advance of SKA1. Although KAT-7 is not equipped with a hydrogen maser, typically required for VLBI observations, we obtained fringes between a single KAT-7 antenna and the 26-metre antenna located at HartRAO near Johannesburg, South Africa. The local GPS-disciplined rubidium time source was deemed sufficient for this experiment. A short 10-second test observation of the bright source 3C273 was performed on 2010 November 23. This involved HartRAO recording the data to their Mark V VLBI system, and KAT-7 recording to disk using the raw-voltage capture system.

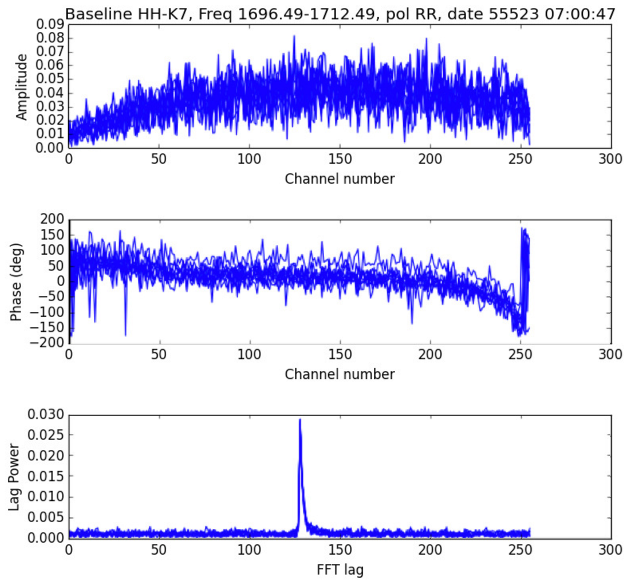

Figure 15. VLBI fringes obtained between KAT-7 and HartRAO using DiFX software correlator. Nine 1.024 second dumps are shown. The horizontal axis is frequency channel and the plots in descending order are visibility amplitude, phase (in degrees) and lag.

Due to the sampling clock of KAT-7 not being a power of 2, we used a DDC (digital down-converter) to convert the sample rate in order to produce the resultant 16 MHz bandwidth, via CUDA code deployed to a GPU.

The data were combined and reduced using in-house python scripts to find the initial position and delay-offset values for the baseline. The data were then combined using the DiFX correlator package with a integration time of 1.024 seconds and channelised with 256 channels (Deller et al. 2007). Strong fringes were subsequently detected as shown in (Figure 15).

9.5 Spectral Lines: HI and OH observations

9.5.1 HI

The receiver on KAT-7 covers the 1420 MHz transition of neutral hydrogen (HI) redshifted as far as 1200 MHz (z=0.184), although the intrinsic faintness of the spectral line and the resolution of the telescope make it most suitable to emission-line studies in the nearby universe. In particular, KAT-7 is well suited for the study of nearby southern objects which have emission on scales larger than 15′, typically invisible to telescopes such as the VLA that lack the short baselines. This was first illustrated in the KAT-7 HI observations of NGC 3109 (Carignan et al. 2013), where 40% more HI flux was detected than in previous VLA measurements (see Figure 16). Observations of NGC 3109 and the dwarf galaxy

[11] An upcoming publication will discuss online de-dispersion and data processing and associated pulsar science with KAT-7.

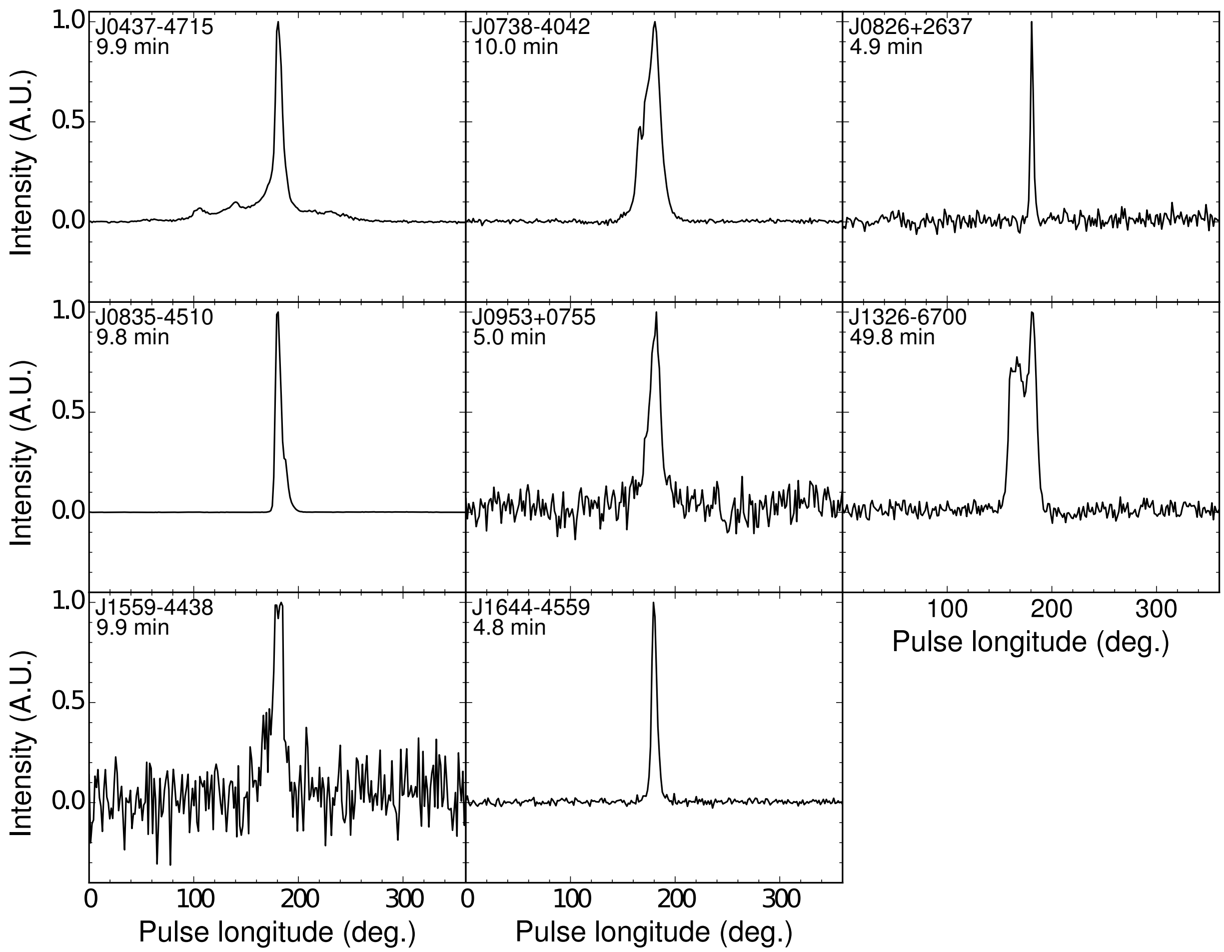

Figure 14. Average profiles for KAT-7 half-band observations of the pulsars J0437−4715, J0738−4042, J0826+2637, J0835−4510, J0953+0755, J1326−6700, J1559−4438 and J1644−4559. These observations were obtained between 2014 August 25 and 2015 April 24 at a centre sky frequency of 1822 MHz. The observation durations are indicated in each of the respective subplots. The data were averaged across the frequency band and folded at the pulsar periods to produce average pulse profiles as a function of rotational phase.

Antlia were carried out over 13 observing sessions between 2012 November 20 and 2012 December 26 using the 'HI galaxies' correlator mode (see table 2) while this was being commissioned. Three fields were positioned in a straight line and extending slightly to the SE to mosaic the region between NGC 3109 and Antlia, covering roughly a region of 2.5°by 1°on the sky. Each field was observed for 25 hours resulting in an r.m.s. noise of 3.7 mJy beam^{-1} in a 1.28 km s^{-1} channel. The new data also allowed the derivation of the rotation curve 16′ further out than the previous VLA measurements (see Figure 10 of Carignan et al. (2013)). A detailed look at the data during calibration led to the discovery of a source of antenna-dependent, faint, very narrow, internally-generated RFI that was successfully eliminated by the insertion of a low-pass filter along the signal path.

The wide field-of-view of KAT-7 and wide-bandwidth spectral-line modes also make it a powerful instrument for mosaicing large areas on the sky, competitive with ATCA in terms of total observing time for similar sensitivity. As part of commissioning the 25 MHz 'HI Galaxy Clusters' spectral-line correlator mode, several projects to image the HI emission in galaxy groups and clusters are currently underway (e.g. Antlia Cluster, NGC 4055 Group). In particular, the Antlia Cluster was observed for 147 hours in a 7-pointing discrete hexagonal mosaic, covering roughly $4.4\mathrm{deg}^2$, and reaching $0.97\mathrm{mJy\,beam}^{-1}$ over the $15.5\mathrm{km\,s}^{-1}$ channels (see Figure 17). This deep map detected 37 HI cluster members, 35 of which were new HI detections, and 27 of which were the first redshift measurements at any wavelength. The broad bandwidth coverage, and lack of bright, dominating sources in the Antlia mosaic led to the recognition of the '$u = 0$' problem in KAT-7 spectral-line data. In this case, RFI that exists below the level of the noise in the visibility data, and would normally be incoherent, adds constructively when the fringe rate between two antennas is equal to zero. It is not a unique phenomenon to KAT-7, but it is particularly a problem on short baselines. (See Hess et al. (2015) for a more complete explanation).

9.5.2 OH

The frequency range of KAT-7 covers all four ground-state transitions of hydroxyl: 1612, 1665, 1667 and 1720 MHz. Maser emission occurs in these transitions under a variety of conditions: in massive star-forming regions (primarily in the main-lines at 1665

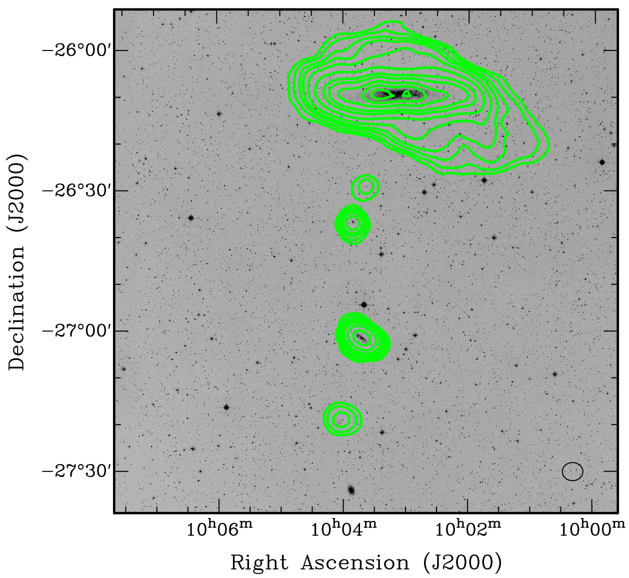

Figure 16. HI mosaic of NGC 3109 and Antlia dwarf superposed on a DSS B image. The green contours are [0.5, 1.07, 2.1, 3.2, 5.4, 10.7, 21.4, 32.2, 53.6, 75.0, and 96.5] times the peak of 107.2Jy $\mathrm{beam}^{-1} \times \mathrm{km\,s}^{-1}$. NGC 3109 ($V_{sys} = 404\,\mathrm{km\,s}^{-1}$) is at the top and Antlia ($V_{sys} = 360\,\mathrm{km\,s}^{-1}$) is at the bottom. The two background galaxies ESO 499-G037 ($V_{sys} = 953\,\mathrm{km\,s}^{-1}$) and ESO 499-G038 ($V_{sys} = 871\,\mathrm{km\,s}^{-1}$) with its associated HI cloud ($V_{sys} = 912\,\mathrm{km\,s}^{-1}$) are between NGC 3109 and Antlia. The synthesized beam is shown in the lower-right corner. Figure adapted from Carignan et al. (2013)

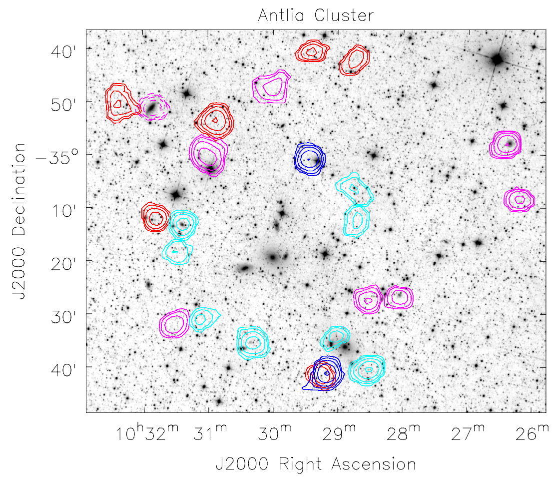

Figure 17. A cut-out of the Antlia Cluster mosaic: color contours corresponding to the systemic velocity of the galaxy detected in HI emission are overlaid on a WISE 3.4 μm image. NGC 3281, detected in absorption, is in dashed contours. Dark blue is $< 2200\,\mathrm{km\,s}^{-1}$, cyan is $2200 - 2800\,\mathrm{km\,s}^{-1}$, magenta is $2800 - 3400\,\mathrm{km\,s}^{-1}$, and red is $> 3400\,\mathrm{km\,s}^{-1}$. HI rich galaxies are detected in a ring around the dominant elliptical galaxy, NGC 3268. These KAT-7 observations had a usable bandwidth sensitivity to HI emission at recessional velocities between $1200 - 4600\,\mathrm{km\,s}^{-1}$, and 37 HI galaxies were detected between $1800 - 4300\,\mathrm{km\,s}^{-1}$. Figure adapted from Hess et al. (2015)

and 1667 MHz (Caswell 1998), in the shells around AGB stars at 1612 MHz (Sevenster et al. 1997), and in shocked regions such as supernova remnants at 1720 MHz (Wardle & Yusef-Zadeh 2002).

While KAT-7 does not have the angular resolution to map individual maser spots, its narrowest spectral mode gives a velocity resolution of 68 m/s, enough to resolve narrow maser lines in massive star-forming regions. A number of methanol masers in star-forming regions have been found to exhibit periodic variations (Goedhart et al. (2014) and references therein). Green et al. (2012) attempted to monitor a short-period source in the hydroxyl mainlines and found a weak indication of periodicity, but the time-series was undersampled. Thus monitoring is an ideal niche application for KAT-7 since it generally has more time available than the Parkes Telescope or ATCA. Six of the known periodic methanol masers have hydroxyl maser counterparts that can be detected with KAT-7. These sources are being monitored on a weekly basis at both 1665 and 1667 MHz, using interleaved observations at both frequencies in a 13-hour schedule block.

Figure 18 shows a pilot observation, carried out on 2013 February 22, of the star-forming region G331.13-0.24 at 1665 MHz. The large field-of-view of KAT-7 led to the detection of several maser sources as well as several diffuse HII regions. The positions, velocities and flux densities are consistent with those from recent Parkes observations (Caswell et al. 2014), confirming that the system is performing as expected. The observations are dynamic-range-limited and three of the six fields observed (including G331.13-0.24) are dominated by off-axis sources, potentially creating errors in the measured flux density of the target source. Direction-dependent calibration techniques are still under investigation (Bhatnagar et al. 2013). Preliminary results from the fields not affected by these effects show significant variability (Goedhart S., van Rooyen R. van der Walt D.J.,Maswanganye J.P., Gaylard M.J. in preparation). The r.m.s. noise after continuum subtraction is typically 0.15 Jy per 381 Hz channel after 50 minutes of integration time. Observations centered on G330.89-0.36, which had a peak brightness of 824 Jy per beam, were used to measure the spectral dynamic range and channel isolation. The total time on source for this observation was 3.95 hours and an r.m.s. noise level of 75 mJy was achieved in line-free channels in the continuum-subtracted data cube. The line-to-line dynamic range was 31 dB. A maximum imaging dynamic range of 32 dB was achieved after applying self-calibration and CLEANing interactively.

10 SUMMARY

We learned several lessons during the construction and use of the KAT-7 array. Here we enumerate the technological lessons learned and their impact on MeerKAT design, and summarize the unique science results captured during scientific commissioning.

10.1 Technology Lessons Learned

The lightweight Stirling coolers used for the cryogenic system are cheaper than conventional Gifford-McMahon (G-M) cycle coolers but need maintenance (at least) annually. They are not cold enough (80 K) to achieve a large cryopumping effect and so the system needs ion pumps in order to retain a high vacuum and mechanical dampers to reduce the vibration generated by the Stirling cool-

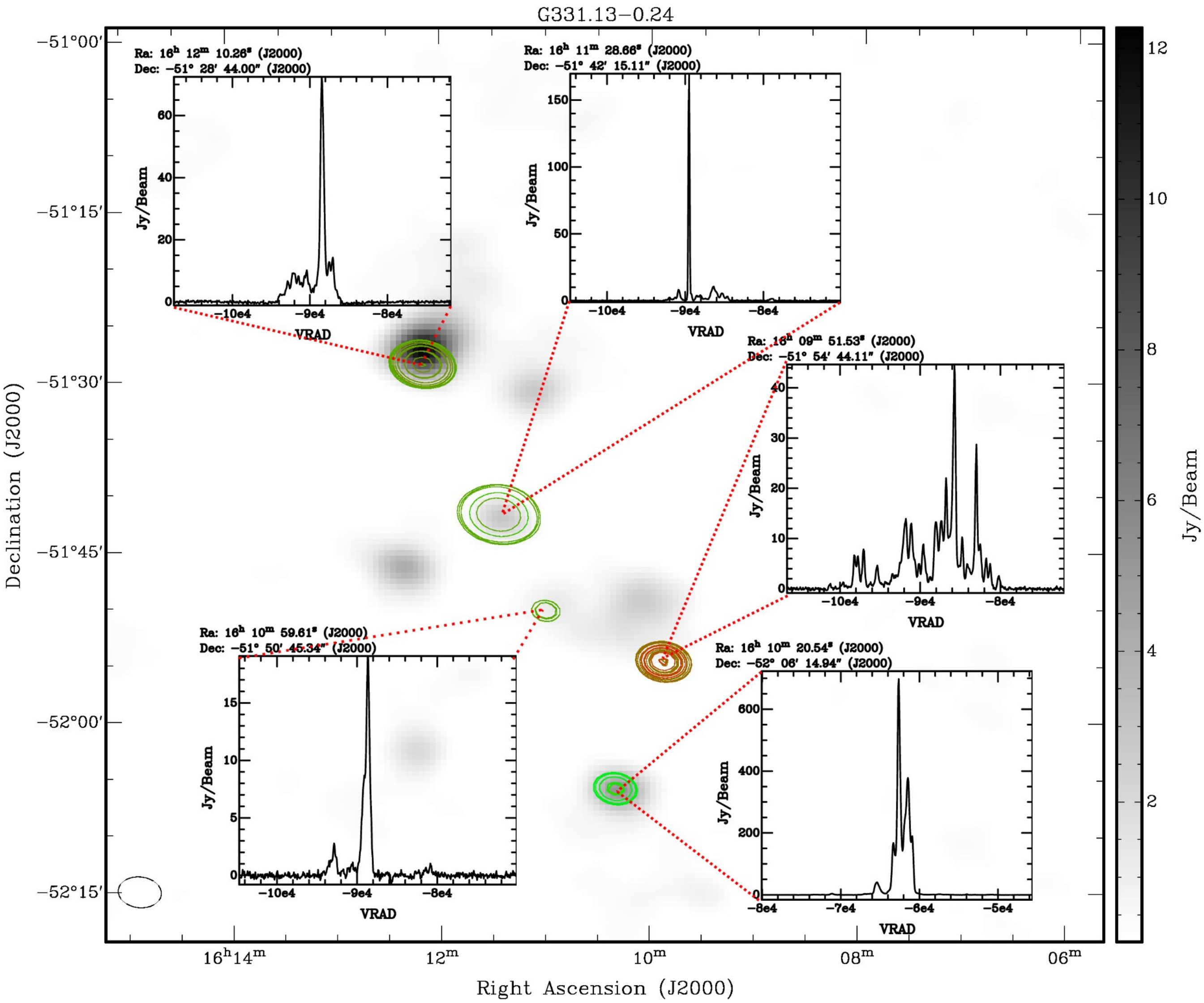

Figure 18. Masers in G331.13-0.24 at 1665 MHz monitored with KAT-7. The underlying greyscale map shows the positions of the continuum emission while the coloured contours show the continuum-subtracted maser emission. The insets show the spectrum at the indicated positions, where the radial velocity scale is $\mathrm{m\,s^{-1}}$ with respect to the Local Standard of Rest. The synthesized beam is shown as a dashed ellipse at the bottom left corner. Primary beam correction was not applied.

ers. Both of these sub-systems need replacement on a regular basis, which involves the use of cranes and a team of technicians, plus about 2 days on an external pump to obtain high enough vacuum before the receivers can be used. The capital expenditure for Stirling cycle cooling for 3 receivers on all 64 MeerKAT antennas is ZAR (South African Rand) 3.3 million less, but the cost of expected maintenance, parts and electricity bill would be ZAR 1.1 million more. This means that over a 3-4 year period Stirling cycle coolers would end up much more expensive to install and operate than G-M cryogenic coolers. Using the G-M cooling system should also reduce down-time for MeerKAT antennas and this has not been factored into the costs.

The composite dishes with embedded metal mesh have large weight advantages over dishes made of large metal panels which in turn means that the backing structure can be light and the motors need not be powerful. They must be constructed correctly as they cannot be adjusted or machined after the fact, and this in turn means that the fibre weave, temperature, humidity and vacuum need to be very carefully controlled during fabrication. Also, the mould needs to be machined to higher accuracy than is needed for the dish; this is relatively simple for a circularly symmetrical design, as only one segment has to be accurately made and then copied. This is far more difficult for a design without that symmetry (e.g. MeerKAT). Large single-piece dishes must be made on-site as moving them becomes a logistical problem.

The ball-screw mechanism for the elevation drive has proven reliable and simple and it is retained in the MeerKAT design.

The KATCP protocol has shown itself to be flexible and very useful in testing and commissioning, and can readily be put into scripting form for routine observations.

SPEAD, although still undergoing active development, has also proven effective and will be further rolled out for use in MeerKAT.

The correlator architecture, correlator and beamformer based on FPGA technology and data transfer over a managed network switch, have also been found to be both flexible and reliable.

10.2 Commissioning science results

Through commissioning we have found that KAT-7 is well suited to observations addressing a diverse range of scientific interests. The telescope's strengths include mapping extended sources in both continuum and spectral-line emission, monitoring variable sources, conducting high time0resolution observations. In particular, the scientific results from KAT-7 commissioning include:

- mapping low-surface-brightness continuum emission (e.g. radio halos and relics, and supernova remnants);
- mapping extended spectral-line sources, such as HI around nearby galaxies, and the large scale structure around galaxy clusters;
- high frequency resolution of OH maser emission around starforming regions;
- observing the variability of continuum sources $\geq$ 10 mJy at 1.8 GHz;
- high time-resolution pulsar observations with the beamformer output;
- VLBI observations with the beamformer output.

For continuum sources we reach a confusion limit of about 1 mJy after 8 hours (@1822 GHz), depending on the field. The confusion limit makes high-dynamic-range imaging difficult, although dynamic ranges of a few thousand are regularly reached. For spectral-line observations, this confusion limit is not an issue. Finally, KAT-7 has pioneered African VLBI observations in combination with HartRAO, in preparation for the SKA.

11 ACKNOWLEDGEMENTS

The SKA South Africa project was formed in 2004 and is funded by the South African Department of Science and Technology (DST), and administered by the National Research Foundation (NRF).

We would especially like to acknowledge the help of the Adam Deller and Walter Brisken with running the DiFX correlator package. Jonathan Quick helped with running the HartRAO VLBI system for the other end of the VLBI test.

We would also like to thank the unnamed reviewer of this paper who suggested many improvements.

REFERENCES

Armstrong R. P., Fender R. P., Nicolson G. D., Ratcliffe S., Linares M., Horrell J., Richter L., Schurch M. P. E., Coriat M., Woudt P., Jonas J., Booth R., Fanaroff B., 2013, MNRAS, 433

Backer D. C., Fisher J. R., 1974, ApJ, 189, 137

Bhatnagar S., Rau U., Golap K., 2013, ApJ, 770, 91

Carignan C., Frank B. S., Hess K. M., Lucero D. M., Randriamampandry T. H., Goedhart S., Passmoor S. S., 2013, AJ, 146, 48

Carretti E., Brown S., Staveley-Smith L., Malarecki J. M., Bernardi G., Gaensler B. M., Haverkorn M., Kesteven M. J., Poppi S., 2013, MNRAS, 430, 1414

Caswell J. L., 1998, MNRAS, 297, 215

Caswell J. L., Green J. A., Phillips C. J., 2014, MNRAS, 439, 1680

Christiansen W. N., Frater R. H., Watkinson A., O'Sullivan J. D., Lockhart I. A., 1977, MNRAS, 181, 183

Ciprini S., Cutini S., 2013, The Astronomer's Telegram, 4770

Curran P. A., Coriat M., Miller-Jones J. C. A., Armstrong R. P., Edwards P. G., Sivakoff G. R., Woudt P., Altamirano D., Belloni T. M., Corbel S., Fender R. P., Körding E. G., Krimm H. A., Markoff S., Migliari S., Russell D. M., Stevens J., Tzioumis T., 2014, MNRAS, 437, 3265

D'Ammando F., Pucella G., Raiteri C. M., et al. 2009, A&A, 508, 181

D'Ammando F., Raiteri C. M., Villata M., et al. 2011, A&A, 529, A145

de Villiers M., 2007, A&A, 469, 793

Deller A. T., Tingay S. J., Bailes M., West C., 2007, PASP, 119, 318

Donato D., 2010, The Astronomer's Telegram, 2583

Gaylard M. J., Bietenholz M. F., Combrinck L., Booth R. S., Buchner S. J., Fanaroff B. L., MacLeod G. C., Nicolson G. D., Quick J. F. H., Stronkhorst P., Venkatasubramani T. L., 2011, in Proceedings of SAIP2011, the 56th Annual Conference of the South African Institute of Physics An African VLBI Network of radio telescopes. South African Institute of Physics ISBN: 978-1-86888-688-3 available online at http://www.saip.org.za, pp 473–478

Goedhart S., Maswanganye J. P., Gaylard M. J., van der Walt D. J., 2014, MNRAS, 437, 1808

Green J. A., Caswell J. L., Voronkov M. A., McClure-Griffiths N. M., 2012, MNRAS, 425, 1504

Hauser M., Hagen H., Wagner S., 2009, The Astronomer's Telegram, 2103

Hauser M., Hagen H., Wagner S., 2010, The Astronomer's Telegram, 2613

Hess K. M., Jarrett T. H., Carignan C., Passmoor S. S., Goedhart S., 2015, MNRAS, 452, 1617

Hotan A. W., van Straten W., Manchester R. N., 2004, PASA, 21, 302

Kassaye E., 2014, Master's thesis, African Institute of Mathematical Sciences

Lazio T. J. W., Waltman E. B., Ghigo F. D., Fiedler R. L., Foster R. S., Johnston K. J., 2001, ApJS, 136, 265

Longo F., Iafrate G., Hays E., Marelli M., 2009, The Astronomer's Telegram, 2104

Marscher A. P., Jorstad S. G., Larionov V. M., et al. 2010, ApJ Lett, 710, L126

Mauch T., Murphy T., Buttery H. J., Curran J., Hunstead R. W., Piestrzynski B., Robertson J. G., Sadler E. M., 2003, MNRAS, 342, 1117

McMullin J. P., Waters B., Schiebel D., Young W., Golap K., 2007, in Shaw R. A., Hill F., Bell D. J., eds, Astronomical Data Analysis Software and Systems XVI Vol. 376 of Astronomical Society of the Pacific Conference Series, CASA Architecture and Applications. p. 127

Olver A. D., Clarricoats P. J. B., Kishk A. A., Shafai L., 1994, Microwave horns and feeds. IEE Electromagnetic Wave Series 39, ISBN:085298094, IET Press, Michael Faraday House,Six Hills Way, Stevenage, Herts SG1 2AY, UK

Oozeer N., Mauch T., Booth R., 2015, Memorie della Societa Astronomica Italiana, 86, 42

Parsons A. R., Backer D. C., Foster G. S., Wright M. C. H., Bradley R. F., Gugliucci N. E., Parashare C. R., Benoit E. E., Aguirre J. E., Jacobs D. C., Carilli C. L., Herne D., Lynch M. J., Manley J. R., Werthimer D. J., 2010, AJ, 139, 1468

Perley R. A., Butler B. J., 2013, ApJS, 204, 19
Riseley C. J., Scaife A. M. M., Oozeer N., Magnus L., Wise M. W., 2015, MNRAS, 477, 1895
Rottgering H. J. A., Wieringa M. H., Hunstead R. W., Ekers R. D., 1997, MNRAS, 290, 577
Rudge A. W., Milne K., Olver A. D., P. K., 1982, The Handbook of Antenna Design. Peter Peregrinus
Rupen M., 1997, Technical report, VLA Test memorandum 202, `http://library.nrao.edu/public/memos/vla/test/VLAT_202.pdf`. NRAO
Saito S., Stawarz Ł., Tanaka Y. T., Takahashi T., Madejski G., D'Ammando F., 2013, ApJ Lett, 766, L11
Scott P. F., Ryle M., 1977, MNRAS, 178, 539
Sevenster M. N., Chapman J. M., Habing H. J., Killeen N. E. B., Lindqvist M., 1997, A&AS, 122, 79
Subrahmanyan R., Ekers R. D., Saripalli L., Sadler E. M., 2010, MNRAS, 402, 2792
Tingay S. J., Jauncey D. L., King E. A., Tzioumis A. K., Lovell J. E. J., Edwards P. G., 2003, PASJ, 55, 351
USSKA Consortium 2002, Technical report, SKA memo 18, Large N - Small D, `http://www.skatelescope.org/publications/`. SKA
van Straten W., Bailes M., 2011, Publ. Astron. Soc. of Australia, 28, 1
Wardle M., Yusef-Zadeh F., 2002, Science, 296, 2350
White R. L., Becker R. H., Helfand D. J., Gregg M. D., 1997, ApJ, 475, 479
Wright A., Otrupcek R., , 1990, Parkes Catalog, 1990, Australia Telescope National Facility, http://vizier.u-strasbg.fr/viz-bin/VizieR?-source=VIII/15 and http://www.parkes.atnf.csiro.au/observing/databases/pkscat90.html

[1]*Square Kilometer Array South Africa, The Park, Park Road, Pinelands, Cape Town 7405, South Africa*
[2]*Deptartment of Physics, University of Oxford, Parks Road, Oxford OX1 3PU, UK*
[3]*EMSS Antennas, 18 Techno Avenue, Technopark, Stellenbosch 7600, South Africa*
[4]*School of Physics, University of the Witwatersrand, PO BOX Wits, Johannesburg 2050, South Africa*
[5]*Dept. of Astronomy, University of Cape Town, Private Bag X3, Rondebosch 7701 Cape Town, South Africa*
[6]*Netherlands Institute for Radio Astronomy (ASTRON), Postbus 2, 7990 AA, Dwingeloo, The Netherlands*
[7]*Kapteyn Astronomical Institute, University of Groningen, Postbus 800, 9700 AV Groningen, The Netherlands*
[8]*Rhodes University, P.O. Box 94, Grahamstown 6140, South Africa*
[9]*Dept. of Electrical Engineering, University of Cape Town,University Private Bag Rondebosch, 7701 Cape Town, South Africa*
[10]*Hartebeesthoek Radio Astronomy Observatory, P.O.Box 443, Krugersdorp 1740South Africa*
[11]*South African Astronomical Observatory, P.O. Box 9, Observatory 7935,South Africa*
[12]*Department of Physics & Astronomy, University of the Western Cape, Private Bag X17. Bellville 7535, Cape Town, South Africa*
[13]*Station de Radioastronomie de Nançay, Observatoire de Paris, PSL Research University, CNRS, Univ. Orléans, OSUC, 18330 Nançay, France* [14]*National Radio Astronomy Observatory,1003 Lopezville Road, Socorro, New Mexico, 87801,*
[15]*Fuller Theological Seminary, 135 N. Oakland Avenue, Pasadena, California, 91182. U.S.A*
[16]*Skaha Remote Sensing Ltd, 3165 Juniper Dr, Naramata BC V0H 1N1, Canada*